Comparing ray-theoretical and finite-frequency teleseismic traveltimes: implications for constraining the ratio of S-wave to P-wave velocity variations in the lower mantle

Carlos A. M. Chaves[1, 2, #], Jeroen Ritsema[1], and Paula Koelemeijer[3]

[1] Department of Earth and Environmental Sciences, University of Michigan, 1100 North University Ave, Ann Arbor, Michigan, USA.

[2] Departamento de Geofísica, Instituto de Astronomia, Geofísica e Ciências Atmosféricas, Universidade de São Paulo, Rua do Matão 1226, São Paulo, São Paulo, Brasil.

[3] Department of Earth Sciences, Royal Holloway, University of London, Egham, Surrey, TW20 0EX, UK

[#] Corresponding author: Carlos Chaves (calbertomc@usp.br)

Abstract

A number of seismological studies have indicated that the ratio R of S-wave and P-wave velocity perturbations increases to 3–4 in the lower mantle with the highest values in the large low-velocity provinces (LLVPs) beneath Africa and the central Pacific. Traveltime constraints on R are based primarily on ray-theoretical modelling of delay times of P waves (ΔT_P) and S waves (ΔT_S), even for measurements derived from long-period waveforms and core-diffracted waves for which ray theory is deemed inaccurate. Along with a published set of traveltime delays, we compare predicted values of ΔT_P, ΔT_S, and the ΔT_S / ΔT_P ratio for ray theory (RT) and finite-frequency theory (FF) to determine the resolvability of R in the lower mantle. We determine the FF predictions of ΔT_P and ΔT_S using cross-correlation methods applied to spectral-element method waveforms, analogous to the analysis of recorded waveforms, and by integration using finite-frequency sensitivity kernels. Our calculations indicate that RT and FF predict a similar variation of the ΔT_S / ΔT_P ratio when R increases linearly with depth in the mantle. However, variations of R in relatively thin layers (< 400 km) are poorly resolved using long-period data (T > 20 s). This is because FF predicts that ΔT_P and ΔT_S vary smoothly with epicentral distance even when vertical P-wave and S-wave gradients change abruptly. Our waveform simulations also show that the estimate of R for the Pacific LLVP is strongly affected by velocity structure shallower in the mantle. If R increases with depth in the mantle, which appears to be a robust inference, the acceleration of P waves in the lithosphere beneath eastern North America and the high-velocity Farallon anomaly negates the P-wave deceleration in the LLVP. This results in a ΔT_P of about 0, whereas ΔT_S is positive. Consequently, the recorded high $\Delta T_S/\Delta T_P$ for events in the southwest Pacific and stations in North America may be misinterpreted as an anomalously high R for the Pacific LLVP.

Key Words:

Body waves; Composition and structure of the mantle; Seismic tomography; Wave propagation

1 Introduction

The ratio of S-wave velocity variations (i.e., $dlnV_S$) and P-wave velocity variations (i.e., $dlnV_P$) provides an important seismological constraint on the thermochemical structure of the mantle. This ratio is written as $R = dlnV_S / dlnV_P$, where $dlnV_S$ and $dlnV_P$ are perturbations from a 1-D reference model for the mantle, PREM (Dziewonski and Anderson, 1981) in case of this paper. R is related to the bulk modulus and rigidity, which have different sensitivities to thermal and compositional heterogeneity.

A multitude of seismic models indicate that R increases from about 1–1.5 in the uppermost mantle to 3–4 in the lowermost mantle and that R is highest in the so-called large-low-velocity-provinces (LLVPs) in the lower mantle beneath Africa and the central Pacific Ocean (e.g., Robertson and Woodhouse, 1996; Su and Dziewonski, 1997; Masters et al., 2000; Bolton and Masters, 2001; Ritsema and van Heijst, 2002; Antolik et al., 2003; Houser et al., 2008; Della Mora et al., 2011; Koelemeijer et al., 2016; Moulik and Ekström, 2016). Values of R higher than 2.5 were originally used to argue that the LLVPs have distinct compositions (see Garnero et al. (2016) and McNamara (2018) for recent reviews) based on mineral-physics experiments on the effects of temperature on $dlnV_S$ and $dlnV_P$. (e.g., Karato and Karki, 2001; Matas and Bukowinsky, 2007; Brodholt et al., 2007). However, the phase transition of bridgmanite to post-perovskite also influences the behavior of R in D" (e.g., Tsuchiya et al. 2004; Wookey et al., 2005; Koelemeijer et al. 2018). Therefore, it remains unclear whether LLVPs can be uniquely interpreted as thermochemical structures based purely on observations of R (e.g., Bull et al., 2009; Schuberth et al., 2009; Davies et al., 2012, 2015; Koelemeijer et al., 2018).

It is not trivial to estimate R in the mantle from an observational perspective. For example, in the upper mantle $dlnV_P$ is well resolved below subduction zones and regions with dense station coverage. In contrast, the resolution of $dlnV_S$ is superior in oceanic upper-mantle regions as surface waves and most normal modes are primarily sensitive to shear-wave velocity. In the lower mantle, shear-wave diffractions (i.e., Sdiff), reflections off the core-mantle boundary (CMB) (e.g., ScS) and core phases (i.e., SKS, SKKS) are recorded with higher amplitudes and over broader epicentral distance intervals than their P-wave counterparts (i.e., Pdiff, PcP, PKP, PKKP). In addition, data sets of differential traveltimes that provide the best constraints on seismic structure in the deep mantle (e.g. S-SKS and ScS-S), as they are insensitive to errors in the hypocenter and heterogeneity in the crust and upper mantle, are much smaller for P-wave phases and only provide limited sampling of the lower mantle (e.g., Tkalčić and Romanowicz, 2002; Simmons and Grand 2002; He and Wen, 2011).

To accurately estimate R in the mantle it is essential to compare $dlnV_S$ and $dlnV_P$ from joint inversions (e.g., Masters et al., 2000; Antolik et al., 2003; Mosca et al., 2012; Koelemeijer et al., 2016; Moulik and Ekström, 2016). However, it is cumbersome to thoroughly explore modelling trade-offs due to differences in P-wave and S-wave data coverage and differences in the sensitivities of body waves and normal modes to $dlnV_S$ and $dlnV_P$. For example, Koelemeijer et al. (2016) found that teleseismic P- and S-wave delay times point to high values of R in D", whereas normal modes, especially Stoneley modes, are explained best when R decreases from a maximum value of 3–4 near 2500 km depth to 1–2 at the CMB. They suspected this to be due to the neglected finite-frequency effects in their traveltime modelling. To and Romanowicz (2009), Malcolm and Trampert (2011), Schuberth et al. (2012), and Xue et al. (2015) also highlighted the finite-frequency effects on long-period direct and diffracted P- and S-wave waveforms. In addition, Tesoniero et al. (2016) argued that constraints on R from seismic tomography are biased by choices in model parameterization and regularization of the inversion.

In this paper, we address the resolvability of R in the lower mantle and specifically the high value of R in the Pacific LLVP by estimating teleseismic traveltimes from computed spectral-element waveforms for synthetic long-wavelength models of $dlnV_S$ and $dlnV_P$. Our analysis is centered around a collection of recorded traveltime delays of direct and diffracted P and S waves measured at relatively long periods (T > 20 s) described in Section 2. In Section 3, we compare ray-theoretical and finite-frequency predictions of traveltimes for different depth profiles of R to illustrate the resolution of 100-km scale depth variations of R in the lowermost mantle and the applicability of ray theory. In Section 4, we show that independently estimating R in the upper mantle and lower mantle is difficult when the azimuthal data coverage is poor. This is particularly relevant to traveltime studies of the Pacific LLVP. In Section 5, we investigate the effects of the crust on traveltime delays and the dependence of P-wave and S-wave sensitivity kernels on the 1-D reference velocity structure. Finally, we discuss the implications of our results for constraining R and the thermochemical nature of the mantle (Section 6).

2 Global observations of P-wave and S-wave travel time delays

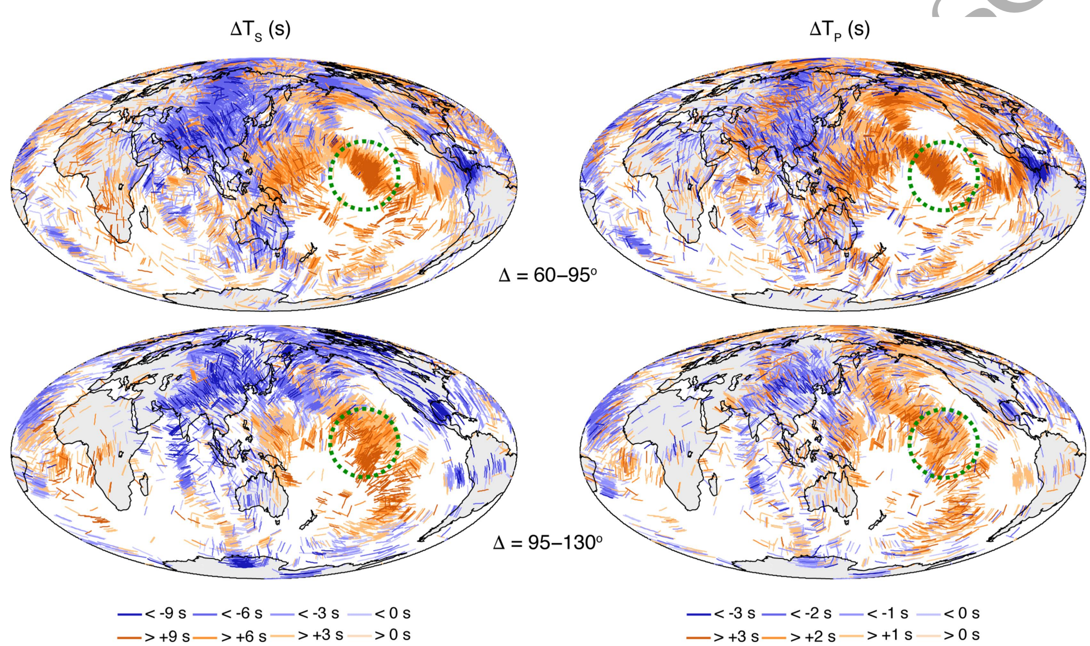

Fig. 1. Measurements of ΔT_S (left) and ΔT_P (right) of teleseismic P and S waves recorded within epicentral distance intervals of Δ = 60–95º (top) and Δ = 95–130º (bottom), corresponding to direct and diffracted waves respectively. The measurements are plotted as 8º-long arcs at the S-wave and P-wave ray turning points and aligned with wave propagation directions. The arcs are blue (or red) if ΔT_P or ΔT_S is negative (or positive). Note that ΔT_S is three times stronger than ΔT_P for arcs with the same color. The green circles indicate the "Pacific data", the focus of this study.

Our analysis is based on 46,500 traveltime anomalies with respect to PREM of direct and diffracted S waves (ΔT_S) and P waves (ΔT_P), which form a subset of those used in the study of Koelemeijer et al. (2016). The traveltime anomalies are recorded for common earthquake-receiver pairs at epicentral distances larger than 60º when P and S waves turn below about 1500 km depth. At distances larger than

95º, P and S waves diffract along the CMB instead. ΔT_S and ΔT_P have been measured by waveform cross-correlation following the procedure outlined by Ritsema and van Heijst (2002). Contributions from the crust, station elevations, Earth's elliptical shape, and earthquake relocations have been subtracted (Ritsema et al., 2011).

When plotted at the ray turning locations (Fig. 1), the variations of ΔT_S and ΔT_P resemble the long-wavelength structure of $dlnV_S$ and $dlnV_P$ in the lower mantle (e.g., Lekić et al., 2012; Koelemeijer et al., 2016). This indicates that seismic heterogeneity in the lower mantle contributes significantly to these delay times at distances larger than 60º. The negative values of ΔT_S and ΔT_P uncover the high-velocity circum-Pacific structure, which is likely related to ancient subduction (e.g., van der Meer et al., 2018). The LLVPs in the lowermost mantle beneath Africa and the Pacific are characterized by delayed S and P waves (i.e., positive values for ΔT_S and ΔT_P). Ray coverage of the Pacific LLVP (indicated by the green circles) is much better than the African LLVP.

Fig. 2 shows ΔT_S plotted against ΔT_P for the same epicentral distance intervals as in Fig. 1. The 46,500 traveltime pairs are divided into two groups. The "Pacific data" include 4,035 measurements for earthquakes in the southwest Pacific recorded at stations in North America. The S and P waves propagate mostly in a northeasterly direction, turning above or propagating through the LLVP beneath the central Pacific Ocean. These data correspond to the measurements highlighted by the green circles in Fig. 1. The "non-Pacific data" are the remaining 42,465 measurements.

In the non-Pacific data set, ΔT_S and ΔT_P vary between about -11 s and +11 s and between about -5 s and +5 s, respectively. The slope of the best-fitting line through these data is 4.8 for Δ = 60–95º (Fig. 2a) and 6.7 for Δ = 95–130º (Fig. 2b). This increase in slope has been used previously to infer that R increases with depth in the mantle (e.g., Masters et al., 2000). The increase of R in the mantle is also clear when comparing SS-wave and PP-wave delays with S-wave and P-wave delays (e.g., Ritsema and van Heijst, 2002).

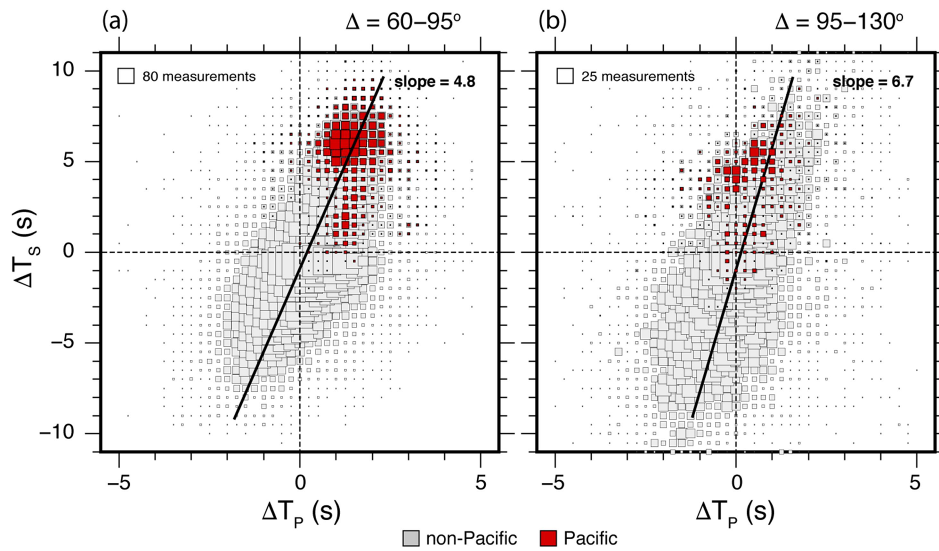

Fig. 2. Measurements of ΔT_S (along the y-axis) and ΔT_P (along the x-axis) for common source-receiver combinations for epicentral distance ranges of (a) Δ = 60–95º and (b) Δ = 95–130º. The non-Pacific measurements are shown using grey squares. The best-fitting lines through these data have been determined by principal component analysis to account for uncertainties in both ΔT_S and ΔT_P, with the values of the slopes indicated to the right. The Pacific data are shown using red squares. The size of each square is proportional to the number of measurements. The scale is indicated in the upper left of each panel. See also Fig. 1.

The Pacific data stand out from the non-Pacific data. The median values of the S-wave traveltime delays in the Pacific subset are about +7 s for Δ = 60–95º and about +5 s for Δ = 95–130º. In comparison, the P-wave delays are small (i.e., < 1–2 s), especially for distances larger than 95º. The resulting relatively high ΔT_S / ΔT_P ratio is the primary body-wave traveltime evidence for the relatively high R-value of the Pacific LLVP as discussed in Section 1.

Normalized histograms of ΔT_S, ΔT_P, and the ΔT_S / ΔT_P ratio illustrate further that the Pacific measurements differ from the non-Pacific measurements (Fig. 3). In the non-Pacific data (Fig. 3a), the distributions of ΔT_S and ΔT_P are roughly centered around the same values. When the epicentral distance increases from Δ = 60–95º to Δ = 95–130º, the distributions shift to more negative values but the change in the ΔT_S / ΔT_P ratio from 1.39 to 1.30 is insignificant given the high standard deviations. In the Pacific data (Fig. 3b), the two distributions are offset with respect to each other. In addition, the differences between the two distance intervals are more significant with the ΔT_S / ΔT_P ratio changing from 3.33 for the Δ = 60–95º epicentral distance interval to 5.65 for Δ = 95–130º. However, the standard deviations are large and the distribution for Δ = 95–130º is non-Gaussian because ΔT_S / ΔT_P have opposite signs for a significant portion of the data. A comparison of Figs 2 and 3 further illustrates the large uncertainty in the ΔT_S / ΔT_P ratio and therefore the inferred values for R. For the non-Pacific data, the mean ΔT_S / ΔT_P ratio based on the histograms (Fig. 3) is 1.3–1.4, which is lower than the ratio of 2.6–3.6 based on the line fit to ΔT_S and ΔT_P (Fig. 2). This inconsistency between inferred R values based on different methods has been pointed out before (Koelemeijer et al., 2016; Tesoniero et al., 2016) and adds a significant uncertainty in the modelling of R (e.g., section 3.2).

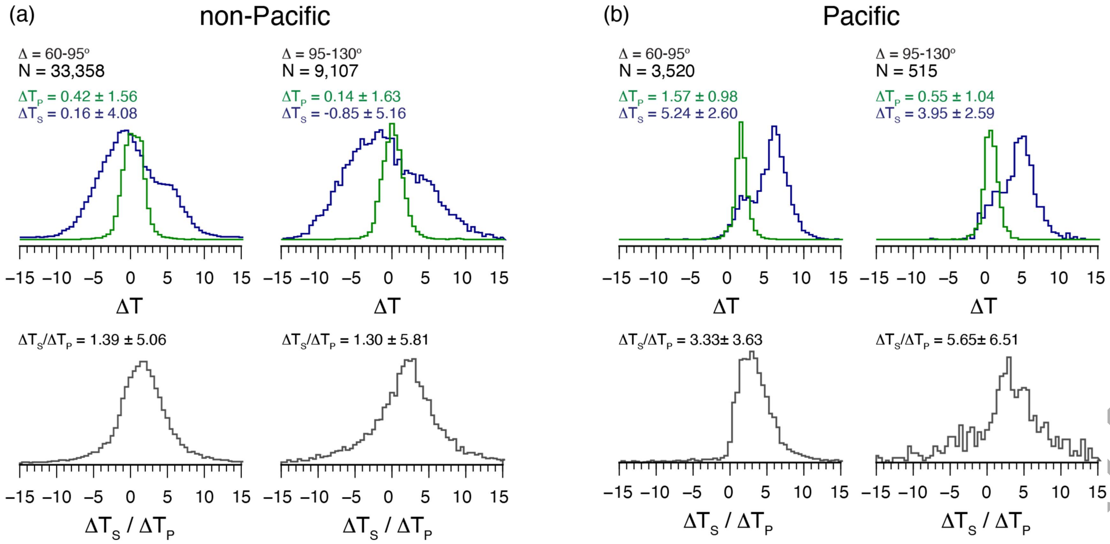

Fig. 3. Normalized histograms of ΔT_S (in green), ΔT_P (in blue), and ΔT_S / ΔT_P (in black) in the a) non-Pacific and b) Pacific data subsets for epicentral distance ranges of (left columns) Δ = 60–95º and (right columns) Δ = 95–130º. Mean values and standard deviations of ΔT_S, ΔT_P, and the ΔT_S / ΔT_P ratio are indicated. N is the number of measurements.

3 The effect of using ray theory or finite-frequency theory

To understand the global observations of the traveltime delays ΔT_S and ΔT_P and the traveltime ratio ΔT_S / ΔT_P discussed in Section 2, we first explore differences between ray-theoretical (RT) and finite-frequency (FF) theory calculations. We predict the traveltime delays for models of $\mathrm{dlnV_S}$ and $\mathrm{dlnV_P}$ with the same lateral variations to simplify our modelling of the depth dependence of R. The $\mathrm{dlnV_S}$ structure is given by model S40RTS (Ritsema et al., 2011) truncated at spherical harmonic degree 12 (Fig. 4a). We call this model S12 from here on. As S12 is similar to the S-wave structure of other long-wavelength shear-wave velocity models (e.g. Ritsema and Lekić, 2020), we do not expect our calculations and conclusions to depend on our choice for S12 to represent large-scale mantle structure. The $\mathrm{dlnV_P}$ structure, which we call P12, is the same as S12 except for a depth-dependent scaling factor R(z), defined as $\mathrm{dlnV_S} = R(z) \times \mathrm{dlnV_P}$. We assume that R is constant or piecewise linear with depth. We do not include crustal structure, but we explore the effects of the crust in Section 5. The source depth is 500 km for all simulations to avoid the influence of depth phases (i.e., pP, sP, sS) on the waveforms and ΔT_S and ΔT_P estimates.

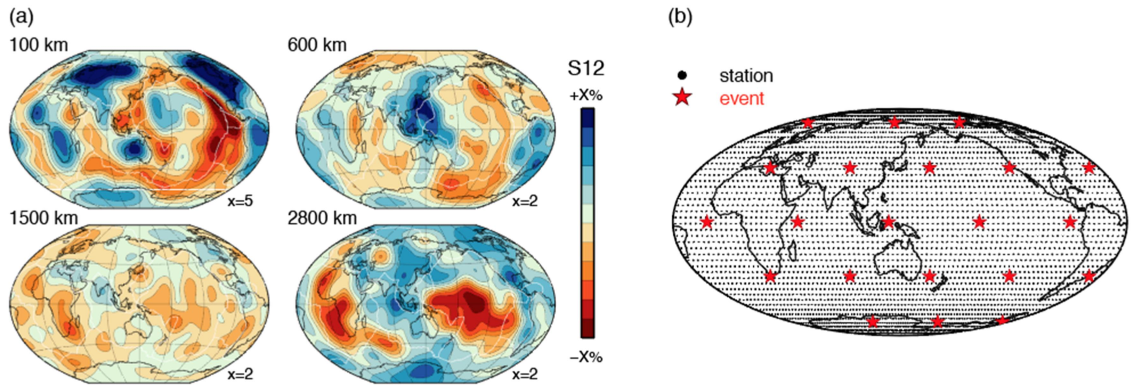

Fig. 4. (a) model S12 at 100 km, 600 km, 1500 km and 2800 km depth and (b) the location of stations (circles) and events (stars) used to calculate synthetic seismograms and theoretical predictions for ΔT_P and ΔT_S.

We determine the ray-theoretical traveltime anomalies by integrating through S12 and P12 along geometric ray paths for an event depth of 500 km. We use the TauP method (Crotwell et al., 1999) and assume that the P-wave and S-wave ray paths can be accurately calculated for the PREM model. In so-called finite-frequency theory, ΔT_S and ΔT_P can be related to $d\ln V_S$ and $d\ln V_P$ via sensitivity kernels K_S and K_P for S waves and P waves, respectively.

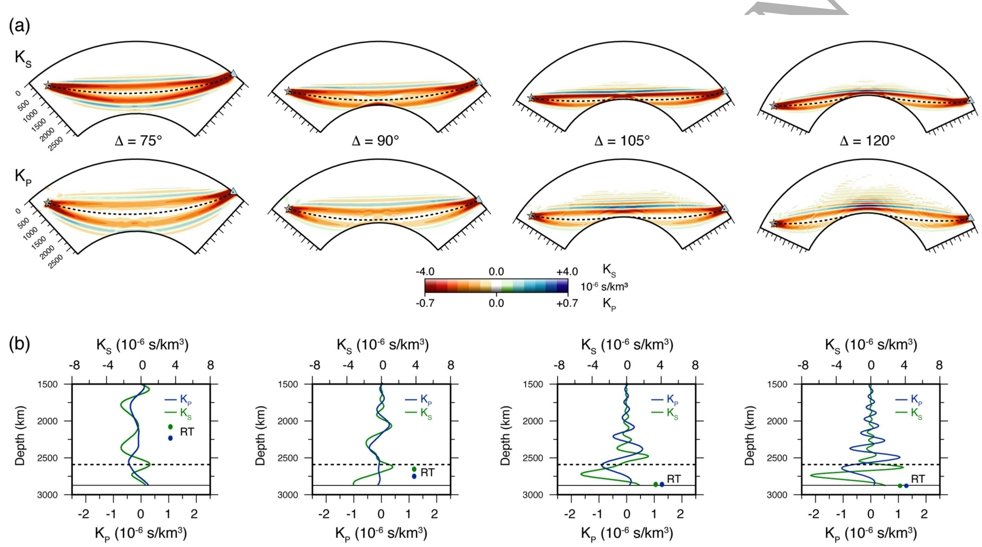

Fig. 5. (a) 2-D cross sections through the finite-frequency traveltime kernels K_S for S waves (top) and K_P for P waves (bottom) computed for the PREM model, a source depth of 555 km, a period of 15 s, and epicentral distances of 75˚, 90˚, 105˚, and 120˚ (from left to right). The dashed lines indicate P- and S-wave ray paths. (b) K_S (in green) and K_P (in blue) as a function of depth along a vertical axis through the wave turning point. Note the different scales used to plot K_S and K_P. The green and blue circles indicate the ray-theoretical turning points of S and P waves, respectively. The solid and dashed horizontal lines are the CMB and a horizon at 300 km above the CMB, respectively.

Fig. 5 shows K_S and K_P for the PREM model computed using the approach by Zhao and Chevrot (2011) and Fuji et al. (2012) combined with normal-mode synthetic seismograms at periods longer than

15 s, equivalent to the period band for which ΔT_S and ΔT_P in our data set (Section 2) have been measured. As described in detail by Hung et al. (2001), the sensitivities of K_S and K_P are zero along the P- and S-wave ray paths. K_S is narrower than K_P because S waves are slower than P waves. Within the first Fresnel zone around the ray path, K_S is stronger than K_P by about a factor of three. When P and S waves diffract at distances larger than 90˚, both K_S and K_P encompass the CMB. K_S peaks closer to the CMB than K_P, indicating that diffracted S waves are more sensitive to velocity heterogeneity at the base of the mantle than diffracted P waves.

We simulate the finite-frequency effects on traveltimes in two different ways. First, we measure traveltime delays from synthetic waveforms and denote the results using the notation FF_{XC}. We compute synthetics with the spectral-element method (SEM, Komatitsch and Tromp, 2002) at periods longer than 7 s for 3-D models of $dlnV_S$ and $dlnV_P$. We measure ΔT_S and ΔT_P by cross-correlating PREM and 3-D waveform segments around the theoretical arrival times. This is a similar approach to the one used to make the measurements described in Section 2, albeit that we use slightly different bandpass frequency bands and adjust the time windows depending on the applied frequency filter.

In a second finite-frequency approach, we estimate the effects on traveltimes by integrating the sensitivity kernels K_S and K_P through S12 and P12, denoting these results using the notation FF_{INT}. To minimise computational cost, we calculate K_S and K_P for the PREM model using the approach by Zhao and Chevrot (2011) and Fuji et al. (2012) at epicentral distance intervals of 1˚, from 40˚ to 120˚ for only one station azimuth and we choose two moment tensors that maximize the radiation of teleseismic S waves and P waves. The traveltimes are then obtained by rotating the sensitivity kernels K_S and K_P, according to each source-station azimuth. Since the computation of synthetic waveforms for hundreds of earthquakes is demanding, we calculate the ray theoretical and the finite-frequency traveltime delays ΔT_S and ΔT_P for a selection of events and receivers, choosing 21 earthquakes and 3,961 stations uniformly distributed around the globe (Fig. 4b). Note that the P-wave and S-wave path coverage is not the same as the coverage in Fig. 1, but it is uniform across the globe.

3.1 Linear increase of R in the mantle

Many studies have found that R increases with depth in the mantle (e.g., Robertson and Woodhouse, 1996; Masters et al., 2000; Ritsema and van Heijst, 2002). In this subsection, we compare RT and FF_{XC} calculations of ΔT_S and ΔT_P for models S12 and P12 with a ratio R that increases linearly from 1 at the surface to 3 at the CMB (R_0 = 1; R_{CMB} = 3). The FF_{XC} calculations are based on cross-correlations of waveforms that have been filtered using a lowpass corner frequency of 0.05 Hz (i.e., a period of 20 s).

Fig. 6a-c compares the RT and FF_{XC} values of ΔT_S and ΔT_P for identical source-receiver pairs for different epicentral distance intervals. P and S waves turn in the lower 1000 km of the mantle for distances smaller than 95˚ and they diffract along the CMB for epicentral distances larger than 100˚. ΔT_S varies more than ΔT_P because $dlnV_S$ is at least a factor of two stronger than $dlnV_P$ in the lower mantle.

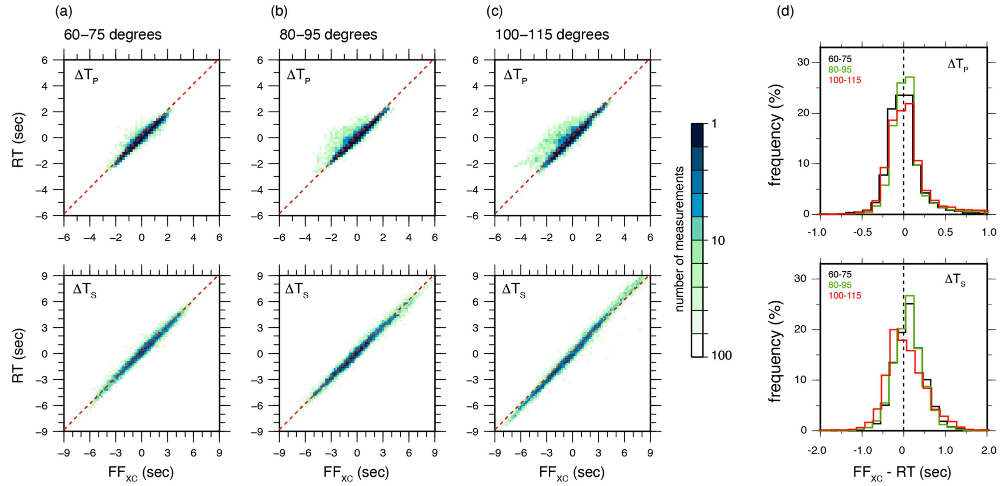

Fig. 6. Ray-theoretical (RT) predictions and finite-frequency (FF_{XC}) predictions (at periods T > 20 s) of ΔT_P and ΔT_S for a profile where $R_0 = 1$ at the surface and $R_{CMB} = 3$ at the CMB. RT values are plotted against FF_{XC} values for ΔT_P in the top panels and ΔT_S in the bottom panels for epicentral distance intervals of (a) 60–75˚, (b) 80–95˚, and (c) 100–115˚. The color in (a), (b), and (c) represents the number of estimates according to the scale shown on the right. The dashed line in each panel is the 1:1 identity line. (d) Frequency histograms of the time difference between the FF_{XC} and RT values of ΔT_P (top) and ΔT_S (bottom) for the distance intervals of panels (a) in black, (b) in green, and (c) in red.

The RT and FF_{XC} values of ΔT_P and ΔT_S agree to within 0.5 s and 1.0 s, respectively as shown in Fig. 6d. The estimates in Fig. 6 farthest from the identity line correspond to S waves and P waves that graze the margins of seismic anomalies so that ΔT_P and ΔT_S are particularly sensitive to the position of seismic anomalies along the ray paths and the geometry of the K_S and K_P sensitivity kernels. The discrepancy between RT and FF_{XC} values of ΔT_P and ΔT_S is relatively large for diffracted waves for two reasons (Fig. 6c). First, the seismic velocity anomalies are strongest at the base of the mantle. Second, the ray theory assumes that P and S waves propagate along the CMB whereas the finite-frequency K_S and K_P kernels have sensitivities throughout D" and maxima well above the CMB (see Fig. 5).

Fig. 7 shows that theoretical predictions for ΔT_S and ΔT_P are correlated and thus that the distance-dependent global average of ΔT_S and ΔT_P and its ratio can be estimated accurately using ray theory for large-scale variations of $dlnV_S$ and $dlnV_P$ and when R varies smoothly with depth. The lines through graphs of ΔT_S and ΔT_P have slopes of 2.7–2.8 for 60–75˚ distance, 3.4–3.5 for 80–95˚ distance, and 3.9–4.1 for 100–115˚ distance. These slopes, determined by principal-component analysis of the estimates in 15˚-wide intervals, have uncertainties smaller than 0.02. The ΔT_S / ΔT_P values for FF_{INT} are slightly higher than for RT and FF_{XC} at distances larger than 60˚, most likely due to simplifications we adopt for calculating K_S and K_P. We assume that the K_S and K_P kernels do not depend on the source mechanism (see Zhao and Chevrot, 2003). The change in sensitivity due to variations in the radiation pattern for different source-receiver azimuths is naturally taken into account in FF_{XC} predictions based on one focal mechanism. However, the increase of ΔT_S / ΔT_P with distance is similar for RT, FF_{XC} and FF_{INT}.

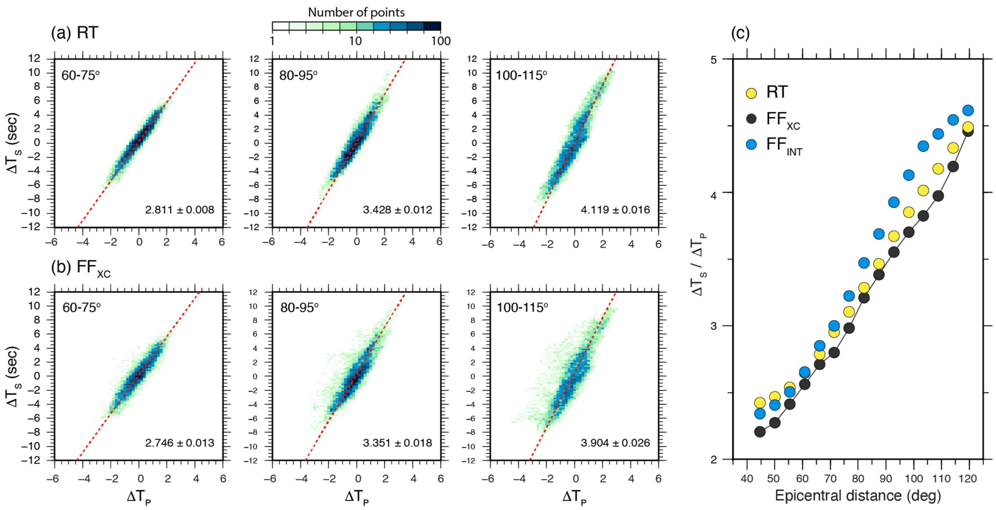

Fig. 7. (a) Ray-theoretical (RT) and (b) finite-frequency (FF_{XC}) calculations (T > 20 s) of ΔT_S (along the y-axis) versus ΔT_P (along the x-axis) for a mantle with $R_0 = 1$ and $R_{CMB} = 3$, shown for epicentral distance intervals of 60–75˚, 80–95˚ and 100–115˚ (from left to right). The red dashed lines are the best-fitting lines through ΔT_S and ΔT_P. Their slopes, determined by principal component analysis, are indicated on the right within each panel. The color of each circle plotted represents the number of estimates according to the scale shown at the top. (c) The ΔT_S / ΔT_P ratio of the FF_{XC} (black circles), FF_{INT} (blue circles) and RT (yellow circles) values as a function of epicentral distance determined for 5˚-wide distance intervals.

3.2 Variations of R within D''

Ray-theoretical and finite-frequency calculations of the ΔT_S / ΔT_P ratio do not agree when the profile of R includes variations on a scale comparable to the width of the K_S and K_P kernels. Fig. 8 illustrates this for two sets of R profiles. In the top panel of Fig. 8, four profiles of R have different slopes in the lowermost 391 km of the mantle (see Fig. 8a). We call this layer D'', but point out that D'' is less than 300 km thick in most seismological studies. For each profile, R increases linearly from R = 1.25 at the surface to R = 4 at the top of D'' (i.e., at 2500 km depth) to resemble the profiles of Koelemeijer et al. (2016). In D'', R is either constant (i.e. $R_{CMB} = 4$), or it linearly decreases to $R_{CMB} = 1$ or 2, or it linearly increases to $R_{CMB} = 7$ or 9. In the bottom panel of Fig. 8, two profiles of R are similar as in Fig 8a but we vary the upper boundary of D" between Z = 2500 km, 2700 km, and 2800 km depth and explore only the extreme values of R at the CMB: $R_{CMB} = 1$ or $R_{CMB} = 9$ (see Fig. 8f).

For either RT or FF (FF_{XC} and FF_{INT}) and for any value of R_{CMB}, the ΔT_S / ΔT_P ratio increases from 3.35 to 4.25 between epicentral distances of 50˚ and 85˚ when P and S waves turn above the D'' layer. For distances larger than 85˚, the RT traveltime predictions track closely the gradient of R in D''. RT predicts that ΔT_S / ΔT_P decreases with distance if R decreases in D'' (i.e., for $R_{CMB} = 1$ and 2) and ΔT_S / ΔT_P increases the fastest when the gradient of R in D'' is strongest (i.e., when $R_{CMB} = 9$). FF_{XC} values of ΔT_S / ΔT_P for the five R profiles in Fig. 8a are closer to one another than for RT, because the sensitivity kernels K_S and K_P are broad in the lowermost mantle. At 120˚, the range of ΔT_S / ΔT_P values decreases with increasing period. It is 3.7 to 7.7 for T > 7 s, but only 4.2 to 6.3 for T > 20 s. Our FF_{INT} predictions of ΔT_S / ΔT_P (Fig. 8c) are higher than FF_{XC} predictions for both period bands due to our modeling simplifications mentioned in section 3.1. The RT and FF predicted variations of the ΔT_S / ΔT_P ratio with distance are similar for $R_{CMB} = 4$ because in this case the R profile is smooth (see also Section 3.1).

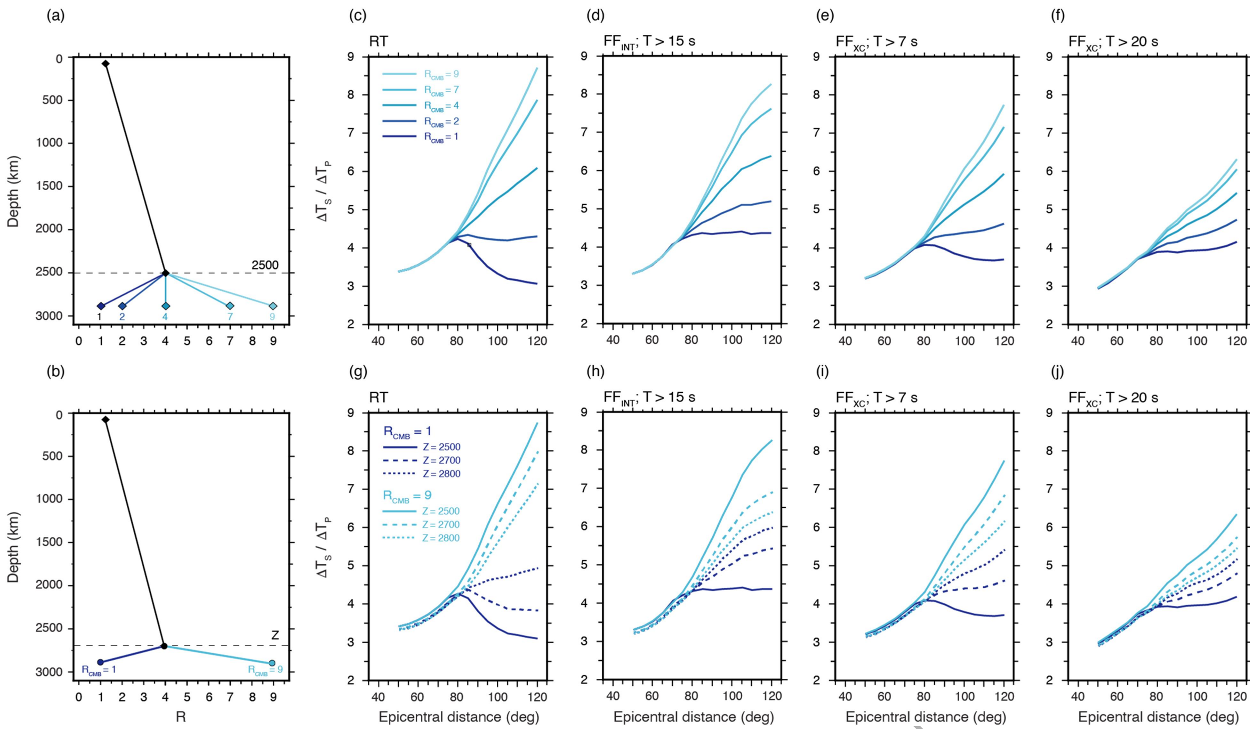

Fig. 8. (a and b) Depth profiles of R composed of two linear segments. For all profiles in (a), R_0 = 1.25 at the Earth's surface and R = 4 at a depth of *z* = 2500 km, mimicking the profiles of Koelemeijer et al. (2016). At the core-mantle boundary, R_{CMB} = 1, 2, 4, 7, or 9. The different segments in D" are shown using different shades of blue. For all profiles in (b), R_0 = 1.25 at the Earth's surface and R = 4 at depths of *Z* = 2500 km, 2700 km and 2800 km. At the core-mantle boundary, R_{CMB} = 1 or 9. (c and g) Ray-theoretical (RT), (d and h) FF_{INT}, and (e, f, i and j) FF_{XC} values of the ratio ΔT_S / ΔT_P as a function of epicentral distance for the profiles of R in (a) and (b). The FF_{INT} results have been obtained by integrating K_S and K_P, determined from normal-mode synthetic seismograms at periods longer than 15 s. The FF_{XC} results in (e) and (i) and in (f) and (j) have been determined using SEM synthetics that have been filtered using lowpass corner frequencies of 0.14 Hz (i.e., T > 7 s) and 0.05 Hz (i.e., T > 20 s), respectively.

Fig. 8f indicates that for traveltime measurements filtered with T > 20 s an increase of the ΔT_S / ΔT_P ratio with distance does not rule out a decrease of R in the lowermost mantle. Based on these results, the increase of the ΔT_S / ΔT_P ratio from 4.8 between 60–95º to 6.7 for 95–120º distance in our traveltime observations (Fig. 2) appears to be best explained when R increases to 9 at the CMB. The average value of R in D" is higher than obtained by Koelemeijer et al. (2016) based on normal-mode data and ray-theoretical modelling of traveltime data. Reconciling the differences requires a rigorous analysis of the data based on FF and for a large number of profiles R.

Fig. 8g–j show a systematic decrease of the range of ΔT_S / ΔT_P ratios for R_{CMB} = 1 or 9 when D" becomes thinner (see Fig. 8b). The RT traveltime predictions still track the gradient of R in D", except when D" is 91 km thick (i.e., Z = 2800 km) and R linearly decreases from R_Z = 4 to R_{CMB} = 1 across D". The FF_{XC} predictions of ΔT_S / ΔT_P ratios tend to converge with increasing periods and as D" becomes thinner. For example, for a 91 km thick D" (i.e., Z = 2800 km), the ΔT_S / ΔT_P values range from 5.5 to 6.2 for T > 7 s, and from 5.2 to 5.5 for T > 20 s at 120˚. This illustrates the difficulty of estimating R in relatively thin (< 100–200 km) layers using long-period body waves due to their sensitivities to a relatively broad depth range. The ΔT_S / ΔT_P estimates for FF_{INT} are higher than for FF_{XC} for any R profile and layer thickness, again due to the maximized sensitivity to the radiation pattern. However the overall behavior of ΔT_S / ΔT_P is the same for FF_{INT} and FF_{XC}.

4 Understanding the high ΔT_S / ΔT_P ratio for the LLVP beneath the central Pacific

Figs 2 and 3 indicate that the measurements of ΔT_S and ΔT_P for S and P waves through the lower mantle beneath the central Pacific (i.e. the Pacific data) form an anomalous subset. Both ΔT_S and ΔT_P drop by about 1 s from the shortest (i.e., 60–95º) to the longest (i.e., 95–130º) distance intervals. ΔT_P has values around 0 s at distances larger than 95º so the ΔT_S / ΔT_P ratio does not have a normal distribution. This would imply that R is anomalously high at the base of the mantle within the Pacific LLVP as interpreted in previous studies (e.g. Masters et al., 2000).

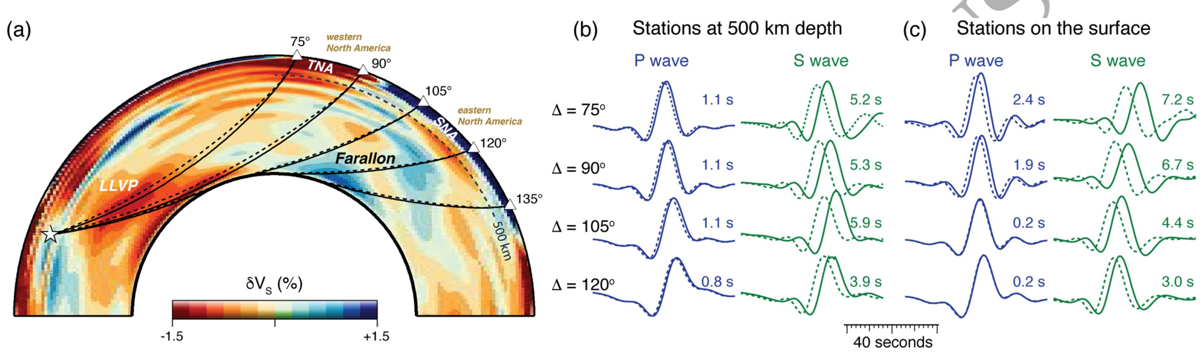

Fig. 9. (a) Vertical cross-section through S12 across the central Pacific and North America. P12 is linearly scaled using R_0 = 1 and R_{CMB} = 3. Superposed are S-wave (dashed lines) and P-wave (solid lines) ray paths between the October 5, 2007 earthquake in the Fiji Islands region (lat = 25.3ºS; lon = 179.5ºE; depth = 540 km) (star) and stations in North America (triangles). The stations are distributed along a linear array between distances of 50° and 140° for a source azimuth of 55°. Hypothetical stations at distances shorter than 75° and longer than 125° are located in the Pacific Ocean and Atlantic Ocean, respectively. The LLVP and Farallon anomalies in the lower mantle and the seismic provinces TNA (tectonic North America) and SNA (stable North America) (definitions from Grand and Helmberger (1984)) in the upper mantle are indicated. The dashed line parallel to the surface is a horizon at 500 km depth. (b) Waveforms of the P-wave (in blue) and S-wave (in green) for PREM (dashed lines) and S12/P12 (solid lines) at distances of 75°, 90°, 105°, and 120°. The numbers to the right of the waveforms are ΔT_S or ΔT_P determined by cross-correlation. Stations are either located (b) at a depth of 500 km or (c) on the surface.

However, unidirectional sampling impedes our ability to constrain R in the lower mantle since $dlnV_P$ in the uppermost mantle is likely to be strong yet poorly constrained compared to $dlnV_S$, as pointed previously by Hock et al. (1997). To illustrate this, we single out the Pacific data, which are mostly based on recordings at stations in North America of earthquakes in the southwestern Pacific, especially the Tonga-Fiji region. The Tonga to North America path (Fig. 9a) includes 3-D velocity structures in the upper and lower mantle that affect the variation of ΔT_S, ΔT_P, and the ΔT_S / ΔT_P ratio with epicentral distance. Observations of epicentral distance variations could thus potentially be misinterpreted as depth variations of R. For the source-receiver geometry of Fig. 9a, wave propagation in the lower mantle is influenced by the Pacific LLVP and the Farallon anomaly, where the shear velocity is up to 2% lower and higher than in the ambient mantle, respectively. The shear velocity in the upper mantle beneath eastern North America (ENA) is even up to 12% higher than in the uppermost mantle beneath western North America (WNA).

To explore how the Pacific LLVP, the Farallon anomaly, and velocity variations in the uppermost mantle beneath North America contribute to ΔT_S and ΔT_P for the Pacific data, we analyze spectral-element-method waveforms for the setup shown in Fig. 9a. The waveforms in Figs 9b and 9c, filtered for periods longer than 20 s, are based on a profile of R with a linear increase with depth from $R_0 = 1$ to $R_{CMB} = 3$. To separate the contributions to ΔT_S and ΔT_P from heterogeneity in the lower mantle and upper mantle, we compute waveforms for stations located at a depth of 500 km (Fig. 9b) and stations on Earth's surface (Fig. 9c). We determine ΔT_S and ΔT_P with respect to PREM by cross-correlating PREM and 3-D waveform segments as discussed before.

The seismically slow LLVP produces a strong S-wave traveltime delay, increasing ΔT_S by nearly 6 s at 105°. At a distance of 120°, the fast Farallon anomaly in the lower mantle reduces ΔT_S to 3.9 s (see Fig. 9b) and the high-velocity upper mantle beneath ENA reduces ΔT_S further to 3.0 s (see Fig. 9c). In contrast, the LLVP and the Farallon anomaly produce smaller ΔT_P perturbations because $d\ln V_P$ is smaller than $d\ln V_S$ in the lower mantle (as $R_{CMB} = 3$). The LLVP only causes a delay in ΔT_P of about 1.1 s, which, after propagating through the Farallon anomaly, is reduced to about 0.8 s at 120° (see Fig. 9b). The high-velocity anomaly in the upper mantle beneath ENA is relatively strong as $R_0 = 1$, reducing the P-wave delay further to about 0.2 s. Hence, the deceleration of the P-wave in the LLVP is as strong as its acceleration in the Farallon anomaly and the upper mantle beneath ENA. As a result, the recorded P-wave traveltime perturbation at surface stations in ENA is small, resulting in anomalously large (> 10) ΔT_S / ΔT_P ratios for diffracted P and S waves that do not relate to variations in R in the lowermost mantle.

5 Additional modelling complications

So far, we have illustrated the influence of the chosen modelling approach (ray-theoretical versus finite-frequency, see Section 3) and the strong effect of upper mantle structure (see Section 4) on estimates of R for the lower mantle. Additional complexities for interpreting global traveltime observations, such as those shown in Section 2, arise from the fact that crustal corrections are commonly applied and sensitivity kernels are computed for a standard reference model, which we explore in more detail now.

5.1 The influence of the crust

Traveltime variations due to crustal heterogeneity can be more than a second and must be determined accurately in order to isolate the effect of the mantle on ΔT_S, ΔT_P, and the ΔT_S / ΔT_P ratio in particular. According to the ray theory, ΔT_S and ΔT_P are proportional to the crustal thickness. However, the delay times inferred from cross-correlation of long-period P- or S-wave waveforms can be different from the ray-theoretical delay times due to the interference between the direct waves and reverberations within the crust.

We illustrate the importance of this effect using five seismic models consisting of a homogeneous crust over a mantle with the PREM velocity structure. In these five models, the crust is 15 km, 20 km, 25 km, 30 km, and 35 km thick, while we use a crustal thickness of 25 km as the reference model. We compute waveforms for periods longer than 15 s and an epicentral distance of 80˚ (Fig. 10). We estimate traveltime differences relative to the reference model using both ray theory and waveform cross-correlation, denoted as Δt_{RT} and Δt_{CC}, respectively. We write the difference between Δt_{CC} and Δt_{RT} as $\varepsilon = \Delta t_{CC} - \Delta t_{RT}$, which represents the systematic error when ray theory is used to estimate delay times due to the crust.

Since the crust is a low-velocity layer, P and S waves arrive respectively earlier and later for models with a thinner and thicker crust compared to the reference model (Fig. 10). The estimated delays for ray-theoretical calculations (Δt_{RT}) and estimates based on waveform cross-correlation (Δt_{CC}) differ by as much as 0.8 s. The error ε tends to be negative for S waves, indicating that the ray theory underpredicts the crustal delay time. For P waves, ε is negative for models with a thinner crust and positive for models with a thicker crust, and crucially, ε is not proportional to changes in crust thickness. Ritsema et al. (2009) found similar trends in ε.

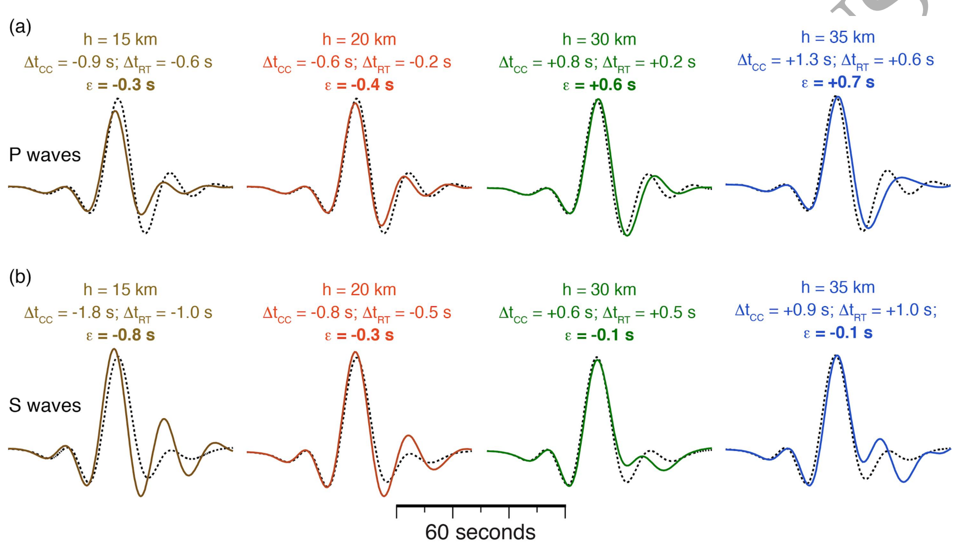

Fig. 10. Spectral-element method waveforms of the P-wave (a) and the S-wave (b) for a seismic reference model with a 25-km thick crust (black dashed lines) and models with a crust that is 15 km (brown solid lines), 20 km (red solid lines), 30 km (green solid lines), or 35 km (blue solid lines) thick. In all models, the crust is homogeneous with a P-wave velocity of 6 km/s and a S-wave velocity of 3.5 km/s. Indicated are the delay times determined by waveform cross-correlation (Δt_{CC}) and ray theory (Δt_{RT}) and their differences (i.e., $\varepsilon = \Delta t_{CC} - \Delta t_{RT}$).

Imprecision in a "crustal correction" of 0.7 s is large compared to the observed ΔT_P (0.8–1.1 s) for the SW Pacific to North America corridor that constrains the LLVP structure beneath the Pacific (see Section 4). If, as has been done in previous work, PREM (with a crustal thickness of 25 km similar to the reference model in Fig. 10) is used and if traveltime delays due to the relatively thick crust (> 35 km) beneath eastern North America are estimated using ray theory, the error ε would significantly bias the estimate of ΔT_P and consequently the ΔT_S / ΔT_P ratio and inferences of R in the lower mantle.

5.2 Dependence of the sensitivity kernels K_S and K_P on 1D-velocity structure

In global tomographic inversions, it is generally assumed that the propagation paths of S and P waves can be computed using PREM. However, P- and S-wave paths may be different when waves traverse the LLVPs, especially near their turning depths. Ritsema et al. (1997) and Thorne et al. (2013) have shown that high amplitudes and sharp waveforms of S waves deep in the core shadow zone can be explained by a shear-wave velocity reduction across D", which forces S waves to turn at a shallower depth in D" and retards the onset of core diffraction to a larger distance than in PREM.

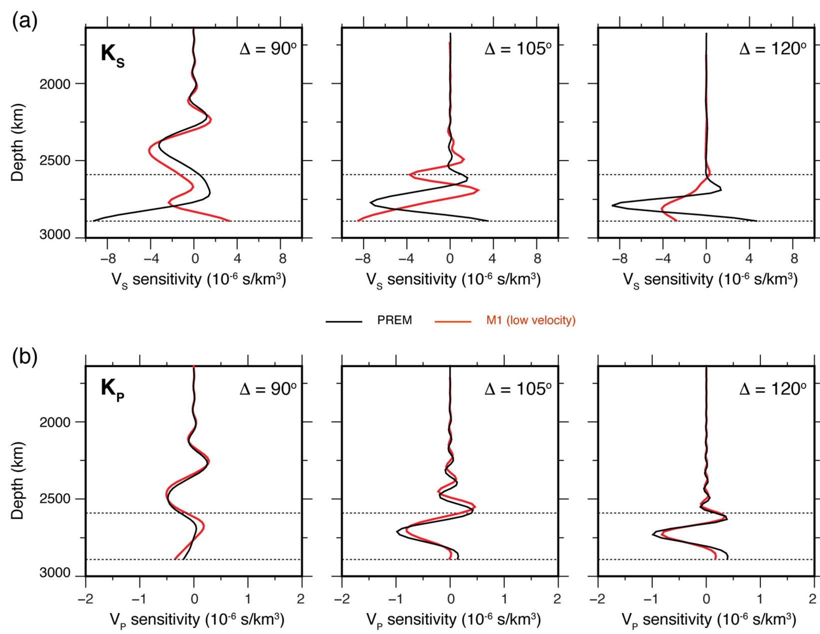

Fig. 11. Sensitivity kernels along a vertical axis through the wave turning point of (a) K_S and (b) K_P for PREM (black lines) and model M1 (red lines) at epicentral distances of 90˚, 105˚, and 120˚ (from left to right). The horizontal lines are the CMB and a horizon at 300 km above the CMB. See also Fig. 5.

A change in the background model also affects the sensitivity kernels K_S and K_P. Fig. 11 compares K_S and K_P computed for PREM and M1 for a period of T = 15 s. In M1 (Ritsema et al. 1997) the P-wave and S-wave velocities decrease in the lowermost 191 km of the mantle to values at the CMB that are 3% lower than in PREM (although there is no observational evidence for such a strong reduction in P-wave velocities). The sensitivity kernel K_P computed for PREM and M1 are similar apart from a minor difference in amplitude, because the sensitivity of P waves to $d\ln V_P$ in the lowermost 200 km of the mantle is relatively small. However, K_S has a different shape and amplitude for PREM and M1. This implies that the S-wave delay time ΔT_S due to a shear-wave velocity anomaly in D" cannot be accurately determined assuming PREM wave paths.

Assuming a profile R = 1 (i.e. $dlnV_P$ and $dlnV_S$ are identical throughout the mantle), the P-wave delay time ΔT_P calculated using K_P in PREM or M1 differs by about 0.1 s and the S-wave delay ΔT_S is about 0.5 s larger when using K_S computed for M1 instead of PREM. These differences are not significant for our analysis of R across the mantle. However, when analyzing relatively thin depth variations (< 200 km) in the lowermost mantle as wide as the sensitivity kernels for M1 and PREM in Fig. 11, it is important to use sensitivity kernels that properly take modified wave propagation paths into account or to use full 3-D synthetic waveforms, as we have done in sections 3-5.

6 Discussion and Conclusions

6.1 Importance of finite-frequency simulations

Most studies of the ratio R (= $dlnV_S$ / $dlnV_P$) in the mantle are based on ray theory. Ray theory is applicable to studies of traveltime measurements based on P-wave and S-wave onsets. However, when traveltimes are derived from the modelling of long-period waveforms and cross-correlation measurements, ray theory is inaccurate as pointed out by numerous researchers (e.g., Wielandt, 1987; Nolet and Dahlen, 2000; Hung et al., 2001). In this paper, we have assumed models for $dlnV_S$ and $dlnV_P$, which are parameterized in the same manner as model SP12RTS of Koelemeijer et al. (2016). For this parameterization, we demonstrate that ray theory can be used to estimate smooth variations of R in the mantle. For example, Fig. 7 shows that ray theory accurately predicts the distance dependence of ΔT_P, ΔT_S, and the ΔT_S / ΔT_P ratio even when the traveltime anomalies have been derived from waveforms with periods longer than 20 s. Therefore, the increase of R in the mantle, consistently determined in numerous studies, is a robust result.

Ray theory is inadequate for resolving variations in R from long-period measurements of ΔT_P and ΔT_S over depth ranges comparable to the vertical widths of the K_P and K_S sensitivity kernels. Due to broad spatial averaging, finite-frequency theory predicts smaller and smoother epicentral distance variations of the traveltime anomalies than ray theory, especially for the longest periods as shown in Section 3.2. Our FF_{INT} predictions of ΔT_S / ΔT_P based on Fréchet kernels for PREM using the normal-mode waveform modelling approach of Zhao & Chevrot (2011) and Fuji et al. (2012) are higher than FF_{XC} based on the cross-correlation of waveforms. This is likely due to simplifications we adopt for calculating K_S and K_P, but we note that the overall behavior of ΔT_S / ΔT_P has remained the same for FF_{INT} and FF_{XC}. Constraining R variations within a 400-km depth range in the mantle requires theories that adequately prescribe the sensitivities of ΔT_P and ΔT_S to $dlnV_S$ and $dlnV_P$ or use full-waveform modelling techniques. Future studies that combine traveltime measurements with normal mode data (such as Moulik and Ekstrom, 2016; Koelemeijer et al., 2016) must thus address differences in the sensitivities to $dlnV_S$ and $dlnV_P$, especially when adopting a relatively fine-scale parameterization in the lowermost mantle, while they should also consider how the presence of anisotropy and dispersion affects constraints on R.

FF calculations are also required to accurately estimate the contributions from the crust to ΔT_S and ΔT_P, as demonstrated in Section 5.1. Ray-theoretical estimates of the crustal contribution to the P-wave traveltime can result in errors as high as 0.7 s for typical thickness variations of the continental crust. This error is large compared to the recorded ΔT_P delays due to lower mantle heterogeneity and should be avoided to attain unbiased estimates of the ΔT_S / ΔT_P ratio. Recent global models S40RTS (Ritsema et al.,

2011) and SP12RTS (Koelemeijer et al., 2016) have incorporated such finite-frequency crustal corrections, while other recent global models have performed joint inversions for the mantle and crustal structure (Bozdağ et al., 2016; Durand et al., 2016; French and Romanowicz, 2014; Lei et al., 2020).

6.2 The ratio R in the Pacific LLVP

In Section 4, we discussed how the variation of the ΔT_S / ΔT_P ratio with epicentral distance could be misinterpreted in regions when azimuthal P-wave and S-wave path coverage is poor. We suggested that the Pacific LLVP produces delays of the P and S waves that are overprinted by the traveltime perturbation in the uppermost mantle beneath North America. The recorded ΔT_P anomaly is small (< 0.2 s) because P-wave acceleration in the high-velocity uppermost mantle beneath eastern North America erases the delay accrued during propagation through the LLVP, resulting in an anomalously high ΔT_S / ΔT_P traveltime ratio (see Fig. 3).

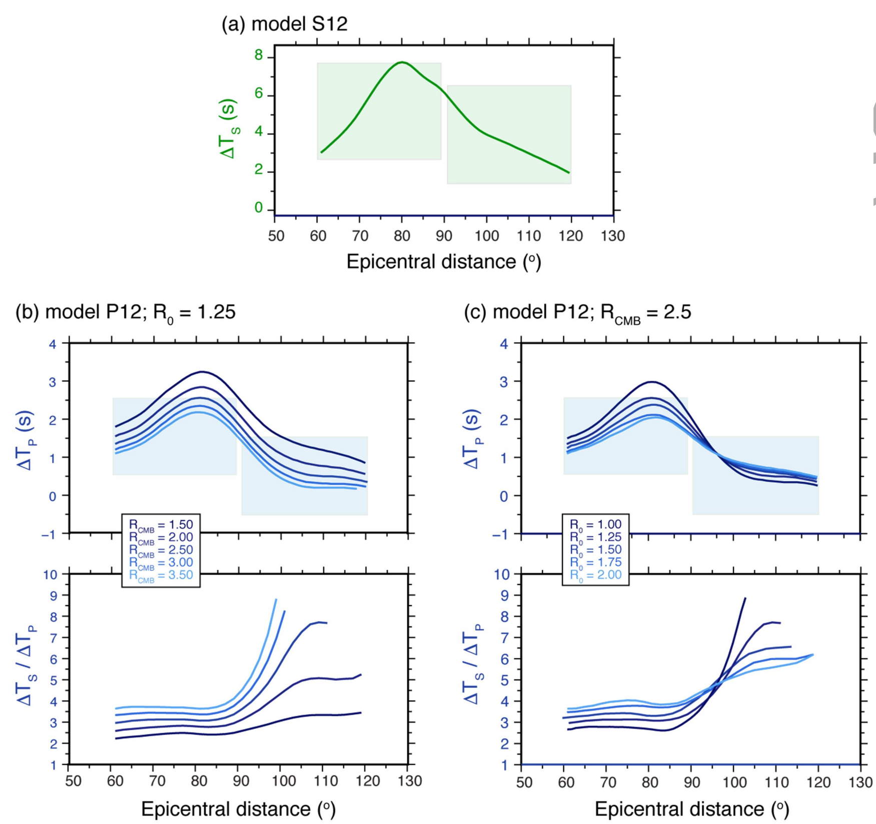

Fig. 12. (a) Predicted values of ΔT_S based on cross-correlation of computed SEM waveforms at T > 20 s for the event and source-receiver geometry from Fig. 9a. The squares indicate the ranges of ΔT_S for the Pacific data for distances smaller and larger than 90° from Fig. 3. (b) Predicted values of ΔT_P top panel) and the ΔT_S / ΔT_P ratio (lower panel) for linear depth profiles of R with R_0 = 1.25 and R_{CMB} varying between 1.5 and 3.5. The squares indicate the ranges of ΔT_P for the Pacific data for distances smaller and larger than 90°. (c) As in (b), but now for linear depth profiles of R with R_{CMB} = 2.5 and R_0 varying between 1.0 and 2.0.

To further investigate the combined effects of the velocity variations in the upper and lower mantle on ΔT_S, ΔT_P, and ΔT_S / ΔT_P, we show in Fig. 12 how traveltime predictions vary for different values of R_0 and R_{CMB} for the same source-receiver geometry as used in Section 4. Fig. 12a shows that model S12 predicts a decrease of ΔT_S with epicentral distance in the Pacific data. Fig. 12b shows that, if $R_0 = 1.25$, as assumed in Section 4, the predicted values of ΔT_P explain the Pacific data within their uncertainty ranges for $R_{CMB} < 3$. Fig. 12c indicates that ΔT_P can also be explained when $R_0 > 1.25$, in other words, if $\mathrm{dln}V_P$ in the upper mantle is slightly weaker than assumed in this study. This further demonstrates the trade-off for constraining R independently in the upper and lower mantle and that it is important to study how uncertainties in surface-wave models of the upper mantle (e.g., Burdick and Lekić, 2017) map into uncertainties in ΔT_P and the ratio R in the lower mantle.

6.3 Implications for the thermochemical structure of the lower mantle

Based on the modelling results from this paper, we argue that the interpretation of LLVPs as compositional distinct structures from teleseismic traveltimes is uncertain. Finite-frequency effects conceal thin layers with anomalous gradients in V_S and V_P and seismic heterogeneity in the lower mantle cannot be distinguished from that in the upper mantle using only teleseismic traveltimes. Although normal-mode based studies, which automatically include finite-frequency effects, also find $R > 2.5$ in the lowermost mantle (e.g. Ishii and Tromp, 2001; Moulik and Ekström, 2016; Koelemeijer et al., 2016), such high R-values and the negative correlation between shear-wave and bulk-sound velocity could also be explained by the phase transition from bridgmanite to post-perovskite (Tsuchiya et al. 2004; Wookey et al., 2005; Davies et al., 2012; Koelemeijer et al., 2018).

In addition to high R-values, other characteristics have been used to infer a chemically distinct origin of the LLVPs. Body-wave waveforms indicate that the LLVPs have strong seismic-wave speed gradients along their margins (Ni et al., 2002; Wang and Wen, 2007; He and Wen, 2012). Normal-mode and solid-earth tide studies suggest that the LLVPs are relatively dense overall (e.g., Ishii and Tromp, 1999; Trampert et al., 2004; Moulik and Ekström, 2016; Lau et al., 2017) or possibly only near the CMB (Koelemeijer et al., 2017) or in parts of the LLVPs (Lu et al., 2020; Koelemeijer, 2020). However, the use of the self-coupling approximation in normal-mode studies of the density structure has been questioned (Al-Attar et al., 2012; Akbarashrafi et al., 2018). This only leaves the tidal tomography study of Lau et al. (2017) as an independent study favouring large-scale dense structures, although it is unclear how their results are affected by the contribution of CMB topography to the excess ellipticity, or whether the same density anomaly can be contained in a thin basal layer (Romanowicz, 2017). Furthermore, sharp sides have also been observed in isochemical models of the LLVPs (Davies et al., 2012). Whether the LLVPs can thus be interpreted uniquely as thermochemical structures remains an open question based on our analysis.

Acknowledgements

The facilities of IRIS Data Services, and specifically the IRIS Data Management Center, were used for access to waveforms, related metadata, and/or derived products used in this study. IRIS Data Services are funded through the Seismological Facilities for the Advancement of Geoscience (SAGE) Award of the National Science Foundation under Cooperative Support Agreement EAR–1851048. All Figures were produced using the GMT software (Wessel et al., 2013). This research has been supported by FAPESP grants 2014/17779–3 and 2016/11580-6 to CC, NSF grant EAR–1416695 to JR, and a Junior Research Fellowship from University College Oxford and a Royal Society University Research Fellowship

(URF\R1\180377) to PK. The authors acknowledge computing time provided on the Blue Gene/Q and DaVinci supercomputers supported by the CRC (Rice University) and LCCA (University of São Paulo) agreement and on the AGUIA supercomputer supported by HPC-STI (University of São Paulo). The SPECFEM3D_Globe software has been provided the Computational Infrastructure for Geodynamics (CIG). All data used in this study are available by contacting the corresponding author at calbertomc@usp.br. We thank editor Ian Bastow, Satoru Tanaka, and an anonymous reviewer for helpful comments.

References

Akbarashrafi, F., Al-Attar, D., Deuss, A., Trampert, J., & Valentine, A. P. (2018), Exact free oscillation spectra, splitting functions and the resolvability of Earth's density structure, *Geophysical Journal International*, 213(1), 58–76, doi:10.1093/gji/ggx539.

Al-Attar, D., Woodhouse, J. H., & Deuss, A. (2012), Calculation of normal mode spectra in laterally heterogeneous earth models using an iterative direct solution method, *Geophysical Journal International*, 189(2), 1038–1046, doi:10.1111/j.1365-246X.2012.05406.x.

Antolik, M., Gu, Y. J., Ekström, G., & Dziewonski, A. M. (2003), J362D28: a new joint model of compressional and shear velocity in the Earth's mantle, *Geophysical Journal International*, 153(2), 443–466, doi:10.1046/j.1365-246X.2003.01910.x.

Bolton, H., & Masters, G. (2001), Travel times of P and S from the global digital seismic networks: Implications for the relative variation of P and S velocity in the mantle, *Journal of Geophysical Research*, 106(B7), 13527–13540, doi:10.1029/2000JB900378.

Bozdağ, E., Peter, D., Lefebvre, M., Komatitsch, D., Tromp, J., Hill, J., Podhorszki, N., & Pugmire D. (2016), Global adjoint tomography: first-generation model, *Geophysical Journal International*, 207(3), 1739–1766, doi:10.1093/gji/ggw356.

Brodholt, J. P., Helffrich, G., & Trampert, J. (2007), Chemical versus thermal heterogeneity in the lower mantle: The most likely role of anelasticity, *Earth and Planetary Science Letters*, 262, 429-437, doi:10.1016/j.epsl.2007.07.054.

Bull, A.L., McNamara, A. K., & Ritsema, J. (2009), Synthetic tomography of Plume Clusters and Thermochemical Piles, *Earth and Planetary Science Letters*, 278, 152-162, doi:10.1016/j.epsl.2008.11.018.

Burdick, S., & Lekić, V. (2017), Velocity variations and uncertainty from transdimensional P-wave tomography of North America, Geophysical Journal International, 209 (2), 1,337–1,351, https://doi.org/10.1093/gji/ggx091.

Crotwell, H. P., Owens, T. J., & Ritsema, J. (1999), The TauP Toolkit: Flexible Seismic Travel-time and Ray-path Utilities, *Seismological Research Letters*, 70(2), 154-160, doi: 10.1785/gssrl.70.2.154.

Davies, D. R., Goes, S., Davies, J. H., Schuberth, B. S. A., Bunge, H.-P., & Ritsema, J. (2012), Reconciling dynamic and seismic models of Earth's lower mantle: the dominant role of thermal heterogeneity. *Earth and Planetary Science Letters.*, 353-354, 253-269, doi:10.1016/j.epsl.2012.08.016.

Davies, D. R., Goes, S. & Lau, H. C. P (2015), Thermally dominated deep mantle LLSVPs: a review. In: The Earth's heterogeneous mantle, Eds. A. Khan, F. Deschamps & K. Kawai. Springer, 441-478, doi:10.1007/978-3-319-15627-9_14.

Della Mora, S., Boschi, L., Tackley, P. J., Nakagawa, T., & Giardini, D. (2011), Low seismic resolution cannot explain S/P decorrelation in the lower mantle, *Geophysical Research Letters*, 38, L12303, doi:10.1029/2011GL047559.

Durand, S., Debayle, E., Ricard, Y., & Lambotte S. (2016), Seismic evidence for a change in the large-scale tomographic pattern across the D″ layer, *Geophysical Research Letters*, 43, 7928–7936, doi:10.1002/2016GL069650.

Dziewonski, A.M. & Anderson, D.L. (1981), Preliminary Reference Earth Model, *Physics of the Earth Planetary Interiors*, 25, 297–356, doi:10.1016/0031-9201(81)90046-7.

French, S. W., & Romanowicz, B. A. (2014), Whole-mantle radially anisotropic shear velocity structure from spectral-element waveform tomography, *Geophysical Journal International*, 199, 1303–1327, doi:10.1093/gji/ggu334.

Fuji, N., Chevrot, S., Zhao, L., Geller, R. J. & Kawai, K. (2012), Finite-frequency structural sensitivities of short-period compressional body waves. *Geophysical Journal International*, 190, 522–540. doi:10.1111/j.1365-246X.2012.05495.x.

Garnero, E. J., McNamara, A. K., & Shim, S. -H. (2016), Continent-sized anomalous zones with low seismic velocity at the base of Earth's mantle, *Nature Geoscience*, 9, doi: 10.1038/NGEO2733.

Grand, Stephen P, & Helmberger, D. V. (1984), Upper mantle shear structure of North America, *Geophysical Journal International*, 76(2), 399–438, doi:10.1111/j.1365-246X.1984.tb05053.x.

He, Y., & Wen, L. (2011), Seismic velocity structures and detailed features of the D″ discontinuity near the core-mantle boundary beneath eastern Eurasia, *Physics of the Earth and Planetary Interiors*, 189(3–4), 176-184,doi:10.1016/j.pepi.2011.09.002.

He, Y., & Wen, L. (2012), Geographic boundary of the "Pacific Anomaly" and its geometry and transitional structurein the north, *Journal of Geophysical Research*, 117, B09308, doi:10.1029/2012JB009436.

Hock, S., Roth, M., & Müller, G. (1997), Long-period ray parameters of the core diffraction Pdiff and mantle heterogeneity, *Journal of Geophysical Research* 102, 17,843–17,856.

Houser, C., Masters, G., Shearer, P., & Laske, G. (2008), Shear and compressional velocity models of the mantle from cluster analysis of long-period waveforms, *Geophysical Journal International*, 174, 195–212, doi:10.1111/j.1365-246X.2008.03763.x.

Hung, S.-H., F. A., Dahlen, & Nolet, G. (2001), Wavefront healing: a banana–doughnut perspective. *Geophysical Journal International*, 146, 289–312. doi:10.1046/j.1365-246x.2001.01466.x.

Ishii, M., & Tromp, J. (1999), Normal-Mode and Free-Air Gravity Constraints on Lateral Variations in Velocity and Density of Earth's Mantle, *Science*, 285(5431), 1231-1236, doi:10.1126/science.285.5431.1231.

Ishii, M., & Tromp, J. (2001), Even-degree lateral variations in the Earth's mantle constrained by free oscillations and the free-air gravity anomaly. *Geophysical Journal International*, 145, 77–96, doi:10.1111/ j.1365-246X.2001.00385.x.

Karato, S., &, Karki, B. B. (2001), Origin of lateral variation of seismic wave velocities and density in the deep mantle, *Journal of Geophysical Research*, 106(B10), 21771–21783, doi:10.1029/2001JB000214.

Koelemeijer, P. (2020). Towards consistent seismological models of the core-mantle boundary landscape, *In press, AGU monograph "Mantle Convection and Surface Expressions", edited by Marquardt, Ballmer, Cottaar & Konter.*

Koelemeijer P., Ritsema, J., Deuss, A., & Van Heijst, H. J. (2016), SP12RTS: a degree-12 model of shear- and compressional-wave velocity for Earth's mantle, *Geophysical Journal International*, 204, doi: 10.1093/gji/ggv481.

Koelemeijer, P., Deuss, A., Ritsema, J. (2017), Density structure of Earth's lowermost mantle from Stoneley mode splitting observations, *Nature Communications*, 8, 15241, doi:10.1038/ncomms15241.

Koelemeijer, P., Schuberth, B. S. A., Davies, D. R., Deuss, A., & Ritsema, J. (2018), Constraints on the presence of post-perovskite in Earth's lowermost mantle from tomographic-geodynamic model comparisons, *Earth and Planetary Science Letters*, 494, 226-238, doi:10.1016/j.epsl.2018.04.056.

Komatitsch, D., & Tromp, J. (2002), Spectral-element simulations of global seismic wave propagation—I. Validation, *Geophysical Journal International*, 149(2), 390-412, doi:10.1046/j.1365-246X.2002.01653.x

Lau, H. C. P., Mitrovica, J. X., Davis, J. L., Tromp, J., Yang, H.-Y., & Al-Attar, D. (2017), Tidal tomography constrains Earth's deep-mantle buoyancy, *Nature*, 551, 321, doi:10.1038/nature24452.

Lei, W., Ruan, Y., Bozdağ, E., Peter, D., Lefebvre, M., Komatitsch, D., Tromp, J., Hill, J., Podhorszki, N. & Pugmire, D. (2020), Global adjoint tomography—model GLAD-M25, *Geophysical Journal International*, 223 (1), 1–21, https://doi.org/10.1093/gji/ggaa253.

Lekić, V., Cottaar, S., Dziewonski, A., Romanowicz, B. (2012), Cluster analysis of global lower mantle tomography: A new class of structure and implications for chemical heterogeneity, *Earth and Planetary Science Letters*, 357–358, 68-77, doi:10.1016/j.epsl.2012.09.014.

Lu, C., Forte, A. M., Simmons, N. A., Grand, S. P., Kajan, M. N., Lai, H., & Garnero, E. J. (2020). The sensitivity of joint inversions of seismic and geodynamic data to mantle viscosity. *Geochemistry, Geophysics, Geosystems*, 21, e2019GC008648. doi:10.1029/2019GC008648.

Nolet, G. & Dahlen, F. A. (2000), Wave front healing and the evolution of seismic delay times, *J. Geophys. Res.*, 105, 19043-19054, 2000. doi:10.1029/2000JB900161.

Malcolm, A. E., & Trampert, J. (2011), Tomographic errors from wave front healing: more than just a fast bias, *Geophysical Journal International*, 185(1), 385–402, doi:10.1111/j.1365-246X.2011.04945.x.

Masters, G. , Laske, G. , Bolton, H. & Dziewonski, A. (2000). The Relative Behavior of Shear Velocity, Bulk Sound Speed, and Compressional Velocity in the Mantle: Implications for Chemical and Thermal Structure. In Earth's Deep Interior: Mineral Physics and Tomography From the Atomic to the Global Scale (eds S. Karato, A. Forte, R. Liebermann, G. Masters and L. Stixrude). doi:10.1029/GM117p0063.

Matas, J., Bukowinski, M. S.T. (2007), On the anelastic contribution to the temperature dependence of lower mantle seismic velocities, *Earth and Planetary Science Letters*, 259(1–2), 51-65, doi:10.1016/j.epsl.2007.04.028.

McNamara, A. K., (2018) A review of large low shear velocity provinces and ultra low velocity zones, *Tectonophysics*, doi:10.1016/j.tecto.2018.04.015.

Moulik, P., & Ekström, G. (2016), The relationships between large-scale variations in shear velocity, density, and compressional velocity in the Earth's mantle, *Journal of Geophysical Research*, 121, doi:10.1002/2015JB012679.

Mosca, I., Cobden, L., Deuss, A., Ritsema, J. & Trampert, J. (2012). Seismic and mineralogical structures of the lower mantle from probabilistic tomography, *Journal of Geophysical Research,* 117, B06304, doi:10.1029/2011JB008851.

Ni, S., Tan, E., Gurnis, M., & Helmberger, D. V. (2002), Sharp sides to the African super plume, *Science*, 296 (5574), 1850 – 1852, doi: 10.1126/science.1070698.

Ritsema, J., & Lekić, V. (2020), Heterogeneity of seismic wave velocity in Earth's mantle, *Annu. Rev. Earth Planet. Sci.* 48(1), 377–401, doi: 10.1146/annurev-earth-082119-065909.

Ritsema, J., Garnero, E., & Lay, T. (1997), A strongly negative shear velocity gradient and lateral variability in the lowermost mantle beneath the Pacific, *Journal of Geophysical Research*, 102(B9), 20395–20411, doi: 10.1029/97JB01507.

Ritsema, J., van Heijst, H.-J. (2002), Constraints on the correlation of P- and S-wave velocity heterogeneity in the mantle from P, PP, PPP and PKPab traveltimes, *Geophysical Journal International*, 149 (2): 482–489. doi: 10.1046/j.1365-246X.2002.01631.x.

Ritsema, J., van Heijst, H. J., Woodhouse, J. H., & Deuss, A. (2009), Long-period body wave traveltimes through the crust: implication for crustal corrections and seismic tomography, *Geophysical Journal International*, 179(2), 1255–1261, doi:10.1111/j.1365-246X.2009.04365.x.

Ritsema J., van Heijst, H. J., Deuss, A., Woodhouse, J. H. (2011), S40RTS: a degree-40 shear-velocity model for the mantle from new Rayleigh wave dispersion, teleseismic traveltimes, and normal-mode splitting function measurements, *Geophysical Journal International*, 184, 10.1111/j.1365–246X.2010.04884.x.

Robertson, G. S., & Woodhouse, J. H. (1996), Ratio of relative S to P velocity heterogeneity in the lower mantle, *Journal of Geophysical Research*, 101(B9), 20041–20052, doi: 10.1029/96JB01905.

Romanowicz, B. (2017). Geophysics: the buoyancy of Earth's deep mantle. *Nature*, 551(7680), 308-309.

Schuberth, B. S. A., Bunge, H. P., & Ritsema, J. (2009), Tomographic filtering of high-resolution mantle circulation models: Can seismic heterogeneity be explained by temperature alone? *Geochemistry Geophysi Geosyst.*, 10, Q05W03, doi: 10.1029/2009GC002401.

Schuberth, B. S. A., Zaroli, C. & Nolet, G. (2012), Synthetic seismograms for a synthetic Earth: long-period P- and S-wave traveltime variations can be explained by temperature alone. *Geophysical Journal International*, 188, 1393–1412. doi:10.1111/j.1365-246X.2011.05333.x.

Simmons, N. A., & Grand, S. P. (2002), Partial melting in the deepest mantle, *Geophysical Research Letters*, 29(11), doi: 10.1029/2001GL013716.

Su, W., & Dziewonski, A. M. (1997), Simultaneous inversion for 3-D variations in shear and bulk velocity in the mantle, *Physics of the Earth and Planetary Interiors*, 100(1–4),135-156, doi:10.1016/S0031-9201(96)03236-0.

Tesoniero, A., Cammarano, F., & Boschi, L. (2016), S−to−P heterogeneity ratio in the lower mantle and thermo-chemical implications, *Geochemistry Geophysics Geosystems*, 17, 2522–2538, doi: 10.1002/2016GC006293.

Thorne, M. S., Zhang, Y., & Ritsema. J. (2013), Evaluation of 1-D and 3-D seismic models of the Pacific lower mantle with S, SKS, and SKKS travel times and amplitudes, *Journal of Geophysical Research*, 118, 985–995, doi:10.1002/jgrb.50054.

Tkalčić, H., & Romanowicz, B. (2002), Short scale heterogeneity in the lowermost mantle: insights from PcP-P and ScS-S data, *Earth and Planetary Science Letters*, 201(1), 57-68,doi:/10.1016/S0012-821X(02)00657-X.

To, A. & Romanowicz, B. (2009), Finite frequency effects on global S diffracted travel times, *Geophys. J. Int.*, 179, 1645-1657, doi:10.1111/j.1365-246X.2009.04359.x.

Trampert, J., Deschamps, F., Resovsky, J., & Yuen, D. (2004), Probabilistic Tomography Maps Chemical Heterogeneities Throughout the Lower Mantle, *Science*, 306, 5697, doi:10.1126/science.1101996.

Tsuchiya, T., Tsuchiya, J., Umemoto, K., & Wentzcovitch, R. M. (2004), Phase transition in $MgSiO_3$ perovskite in the earth's lower mantle, *Earth and Planetary Science Letters*, 224(3–4), 241-248, doi:10.1016/j.epsl.2004.05.017.

van der Meer, D. G., van Hinsbergen, D. J. J., & Spakman, W. (2018), Atlas of the Underworld: slab remnants in the mantle, their sinking history, and a new outlook on lower mantle viscosity, *Tectonophysics*, 723, 309–448, doi.org/10.1016/j.tecto.2017.10.004.

Wang, Y., & Wen, L. (2007), Geometry and P and S velocity structure of the "African Anomaly", *Journal of Geophysical Research*, 112, B05313, doi: 10.1029/2006JB004483.

Wielandt E. (1987), On the validity of the ray approximation for interpreting delay times. In: Nolet G. (eds) Seismic Tomography. Seismology and Exploration Geophysics, vol 5. Springer, Dordrecht, https://doi.org/10.1007/978-94-009-3899-1_4.

Wessel, P., Smith, W. H. F., Scharroo, R., Luis, J. & Wobbe, F. (2013), Generic Mapping Tools: improved version released, EOS Trans. AGU, 94(45), 409–410, doi:10.1002/2013EO450001.

Wookey, J., Stackhouse, S., Kendall, J.-M., Brodholt, J., & Price, G. D. (2005), Efficacy of the post-perovskite phase as an explanation for lowermost-mantle seismic properties, *Nature*, 438, 1004, doi:10.1038/nature04345.

Xue, J., Zhou, Y., & Chen, Y. J. (2015), Tomographic resolution of plume anomalies in the lowermost mantle, *Geophysical Journal International*, 201(2), 979–995.

Zhao, L., & Chevrot, S. (2003), SS-wave sensitivity to upper mantle structure: Implications for the mapping of transition zone discontinuity topographies, *Geophys. Res. Lett.*, 30(11), 1590, doi:10.1029/2003GL017223.

Zhao, L., & Chevrot, S. (2011), An efficient and flexible approach to the calculation of three-dimensional full-wave Fréchet kernels for seismic tomography—I. Theory. *Geophysical Journal International*, 185, 922–938. doi:10.1111/j.1365-246X.2011.04983.x.